The brightness temperature of Mercury at mm-wavelengths

A. Greve, C. Thum, Raphaël Moreno, Nicolas Yan

A&A 495, 639–646 (2009)
DOI: 10.1051/0004-6361:20077165

Astronomy & Astrophysics

The brightness temperature of Mercury at mm-wavelengths

A. Greve[1], C. Thum[1], R. Moreno[1,2], and N. Yan[3]

[1] IRAM, 300 rue de la Piscine, 38406 Saint-Martin d'Hères, France
e-mail: thum@iram.fr
[2] LESIA (LAM – bat. 18), 5 place Jules Janssen, 92195 Meudon Cedex, France
[3] Service d'Aéronomie CNRS/IPSL, 91371 Verrières-le-Buisson, France

Received 25 January 2007 / Accepted 24 November 2008

ABSTRACT

We present observations of Mercury made with the IRAM 30-m telescope at 3, 2 and 1.3 mm wavelength (90, 150 and 230 GHz) during the years 1985−2005; we derive from these data the disk-averaged brightness temperatures. The observations at 3 mm combined with those by Epstein & Andrew allow a separation of the data into 40° wide longitude intervals and by this an investigation of the disk-averaged brightness temperature with Mercury's longitude. From the new mm-wavelength data, and data taken from the literature, we derive the disk-averaged brightness temperature as a function of wavelength. On Mercury's night side a significant decrease in brightness temperature occurs towards shorter wavelengths.
We use the three surface models (A,B,C) discussed by Mitchell & de Pater and calculate for the cool and hot surface region the corresponding diurnal variation of the disk-averaged brightness temperature at 90 GHz. For the same models we calculate the variation of the disk-averaged brightness temperature with wavelength between 1.3 mm and 37 mm, on Mercury's midnight side and noon side. Although the scatter in the observations is large, there seems to be a marginally better agreement with model B and A.

Key words. radio continuum: solar system – planets and satellites: individual: Mercury

1. Introduction

Pictures obtained in spacecraft fly-by missions show that Mercury belongs to the rocky bodies of the solar system, with no atmosphere. The impact shattered surface of Mercury is covered by many craters and several basins, but there are no extended, flat, and dust-covered areas like the Mare regions of the Moon. Because of their global similarity, theoretical studies and models of the Moon have been taken, with some modification, to construct models of Mercury.

Mercury has been observed at radio wavelengths down to 3.3 mm during the years ∼1960 to 1985, thereafter the interest in single-dish observations had somewhat faded (Soter & Ulrichs 1967; Morrison 1970; Klein 1970; Morrison & Klein 1970; Epstein et al. 1970; Epstein & Andrew 1985). Single-dish observations must extend over long time intervals in order to cover the diurnal thermal behaviour of specific surface areas, while interferometer observations (Ledlow et al. 1992; Mitchell & de Pater 1994) provide snapshots of the diurnal cycle with, when specially chosen, the effect of surface areas in sunshine and in shadow. The authors were able to reproduce with model calculations the diurnal variation of the brightness temperature and the observed brightness distribution across the disk, by this constraining the thermal and electrical properties of Merucry's surface material. Observations of Mercury's surface temperature provide information on thermal properties of solar system rock material at high temperatures (∼600 K) and large temperature variations (∼250 K). In addition, Mercury's surface material has a high density and perhaps also a different chemical composition which makes comparative studies with other solar system rock material and the Moon important. Unfortunately, because of the scarcity of short mm-wavelength brightness temperature determinations, a study of Mercury's boundary layer is difficult, although theoretical tools for such studies are available for Mercury (Morrison 1970; Morrison & Klein 1970; Cuzzi 1974; Krotikov & Shchuko 1975; Mitchell & de Pater 1994; Hale & Hapke 2002; Yan et al. 2006) and from similar studies of the Moon (for instance, Krotikov & Troitskii 1964; Linsky 1973; Keihm 1984). In theoretical studies of Mercury we notice a shift in interest, in recent years, to the question of sub-surface water ice, in particular under crater floors (Ingersoll et al. 1992; Salvail & Fanale 1994; Sprague et al. 1995; Vasavada et al. 1999).

Mercury moves on a highly eccentric orbit ($\epsilon = 0.206$) with perihelion and aphelion distances of 0.307 AU and 0.467 AU, respectively. The solar radiation falling on Mercury therefore varies by a factor $(0.467/0.307)^2 = 2.314$, so that the radiation at perihelion and aphelion is 10.6 and 4.6 solar constants. In addition, Mercury's rotation is locked so that 3 sidereal rotations are made during 2 orbital revolutions (Peale 1988). As a consequence, Mercury always directs at perihelion and aphelion the same longitudes towards the Sun, separated by 180°. The subsolar longitudes at perihelion, L_p and $L_p + 180°$, receive on average over 2 orbital revolutions systematically more solar radiation than the rest of the surface, and therefore will be the hottest. Likewise, the regions facing the Sun at aphelion, L_a and $L_a + 180°$, receive on average the smallest amount of solar radiation, and therefore will be the coolest. The orbital eccentricity and the locked rotation divide the planet's surface into two "hot" regions (poles) at opposite sides and two "cold" regions (poles) at right angles, so named since the early discussion of this effect (Soter & Ulrichs 1967). "Warm" surface regions are located at intermediate longitudes. These thermally distinct regions are in addition subject to the daily temperature cycle (with one Hermitian solar day equal to 176 Earth days). Evidently, the temperature of any one of the hot, warm, and cool regions can be measured when they face the Earth.

Article published by EDP Sciences

We report on measurements at 3 mm, 2 mm, and 1.3 mm wavelengths made with the IRAM 30-m telescope during the years 1985 to 2005. Combining our 3 mm data with those of Epstein & Andrew (1985), and accounting for the phase efffect, we derive at 3 mm the variation of the disk-averaged brightness temperature as a function of Mercury's longitude. From the combination of the mm-observations with published longer wavelength observations we are able to derive the midnight and noon brightness temperature as a function of wavelength. We compare the observations with predictions from the models A, B and C used by Mitchell & de Pater (1994).

2. Observations

We analyse single-dish heterodyne observations (0.5 to 1 GHz bandwidth) made between 1985 and 2005 with the IRAM 30-m telescope near 90 GHz (3.3 mm), 150 GHz (2 mm), and 230 GHz (1.3 mm). Most of the data were obtained during pointing measurements. The archived data are extracted from scans across Mercury, and other sources (often down to ∼−15 dB), and include the area of the fitted Gaussian profiles, their halfwidths, their pointing offsets, and their peak antenna temperatures, separately determined for azimuth (AZ) and elevation (EL) direction. An archived measurement is accepted in our analysis if the AZ and EL pointing offsets do not exceed ∼2−5″, i.e. being small compared to the beam width (*FWHP*) of 27″ at 90 GHz, 16″ at 150 GHz, and 11″ at 230 GHz; and if the AZ and EL beam widths are within 3−4″ of the source-convolved value. This selection excludes scans affected by anomalous refraction, which may be strong in particular for observations close to the Sun (Altenhoff et al. 1996; Olmi 2001). Under these conditions the antenna temperatures obtained from the AZ and EL scans agree within 5 to 10%, and their average value is used. The four scans of a pointing measurement give the standard error.

The hot-cold-sky calibration method used at the 30-m telescope corrects for atmospheric attenuation and provides the antenna temperature T_a^* [K]. The aperture efficiency ϵ_{ap} and forward efficiency F_{eff} (see Downes 1989; Greve et al. 1998b) is regularly determined (F_{eff} to within ±5%, ϵ_{ap} to within ±10%) and the flux density of the source, per beam, is $S_b = 2\,(k/A)\,T_a^*\,F_{eff}/\epsilon_{ap} = 3.904 T_a^*\,F_{eff}/\epsilon_{ap}$ [Jy] (with A the geometrical area of the 30-m reflector and k the Boltzmann constant). It is impossible to recover the actual value F_{eff}/ϵ_{ap} for a certain day in order to derive the flux density S_b from the archived antenna temperature T_a^*. However simultaneous observations of the constant[1] sources NGC 7027, NGC 7538, W3OH and K3–50A (see for instance Steppe et al. 1993; Reuter & Kramer 1998; Sandell 1994) were used to derive the gain $S_b/T_a^* = 3.904\,F_{eff}/\epsilon_{ap}$ [Jy/K], which we applied to the observations of Mercury. Table 1 summarizes the precision of repeated 90 GHz measurements of the secondary calibrators. In general, the long-term precision of 90 GHz measurements is 10% or better, and 10 to 20% for 150 GHz and 230 GHz measurements. When necessary, a gain-elevation correction is applied (Greve et al. 1998a).

From the relation between the observed flux density S_b, the temperature $T_B(\theta,\psi)$ of a planet assumed to be radiating as a black-body [$B(T_B)$], the beam pattern $P(\theta,\psi)$, and the solid angle Ω of the planet subtended at the time of observation

$$S_b = \int_0^{\Omega} B[T_B(\theta-\theta',\psi-\psi')]P(\theta',\psi')\mathrm{d}\Omega' \quad (1)$$

we obtain for the Rayleigh-Jeans approximation of the Planck function $B(T_B) = 2\,\nu^2\,kT_{RJ}/c^2$ and the assumption of a constant temperature $T_B(\theta,\psi) = T_B\,\Pi(\theta,\psi)$ across the disk (Π) of the planet

$$S_b = (2\,k/\lambda^2)\,T_B \int_0^{\Omega} \Pi(\theta-\theta',\psi-\psi')P(\theta',\psi')\mathrm{d}\Omega'. \quad (2)$$

We use Gaussian profiles for the wavelength dependent beam patterns $P(\theta,\psi)$ (Greve et al. 1998b), which remained constant throughout the years by using receivers of similar illumination taper. With the temperatures of Mercury in the range of 200 to 700 K the difference between the Rayleigh-Jeans temperature T_{RJ} and the black body temperature T_B is between 0.5 to 3%, over the wavelength range considered here, which is below the accuracy of the observations (∼5−20%). In the following T_B is the disk-averaged brightness temperature calculated from Eq. (2).

Observations at Mercury's upper and lower conjunction are made close to the Sun. Since the flux densities are derived from cross scans and baseline subtraction, the data used here are free from solar radiation in the far side lobes. In addition, the IRAM 30-m telescope is actively temperature controlled (Greve et al. 2005) and experience indicates that the possible beam degradation is very small when observing close to the Sun (≲2°, observing time ≲1 to 2 h). A few observations close to upper conjunction apparently show a real "anomaly", of up to ∼30% (see Fig. 4, hot region), as also mentioned by Epstein & Andrew (1985).

The collected data are binned into frequency/wavelength intervals of 86−115 GHz (3.5−2.6 mm): the 90 GHz region; of 130−160 GHz (2.1−1.9 mm): the 150 GHz region; and 220−250 GHz (1.4−1.2 mm): the 230 GHz region.

Table 1. 90 GHz observations (IRAM 30–m telescope): Precision of repeated measurements of secondary standards.

Source	$\langle T_a^* \rangle$ [K]	rms($T_a^*/\langle T_a^* \rangle$) [%]	Number of Observ.[a]
NGC 7538	0.41(6)	10.0	351
W3OH	0.63(4)	8.1	517
NGC 7027	0.77(2)	8.2	488
K3–50A	1.06(5)	8.7	451

[a] For the years 1985 to 2005.

3. The 90 GHz interval

Because of the 3/2-locked rotation/revolution period, the derived disk-averaged brightness temperature T_B is a function of Mercury's longitude L, with the phase (φ) of Mercury superimposed. In order to obtain statistical significance of the first order approximation

$$T_B = \langle T_B(L) \rangle + \Delta T_B(L)\cos(2\,\pi\,\mathcal{D} - \Omega(L)) \quad (3)$$

(which assumes a homogeneous body of Mercury with no longitude and latitude dependence of the surface properties), Epstein & Andrew (1985) binned their 99 observed 3.3 mm brightness

[1] Due to the flat spectrum of NGC 7027 (Sanchez-Contreras et al. 1998) the reported flux density variation at 1.4 GHz of 0.24%/per year (Perley et al. 2006) also is expected to occur, approximately, at mm-wavelengths. This amounts to a change of ∼5% in 20 years, which is below the accuracy of our measurements. For the other secondary calibrators, if variable at all, no published data are available.

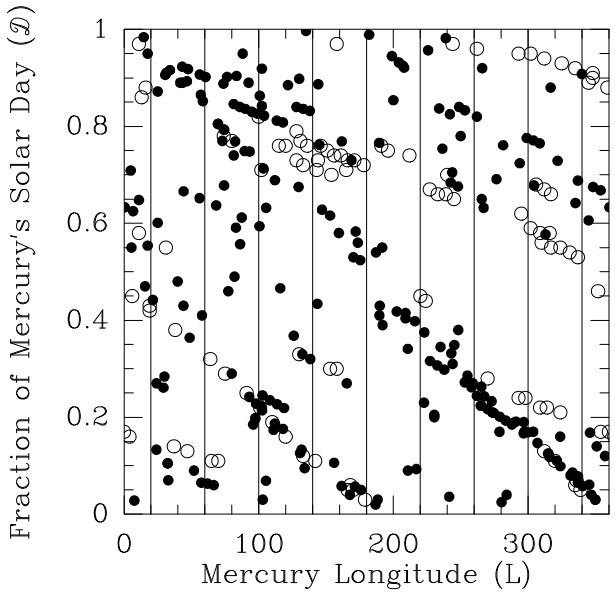

Fig. 1. 90 GHz: coverage in longitude and phase (fraction of Mercury's solar day, Eq. (4)) of our observations: dots, and the observations by Epstein & Andrew (1985): open circles. The width of the intervals is $\Delta L = 40°$.

temperatures into the hot surface regions ($330° \le L \le 30°$ and $150° \le L \le 210°$), the cool surface regions ($60° \le L \le 120°$ and $240° \le L \le 300°$), and the warm surface regions in between. In Eq. (3)

$$\mathcal{D} = 1 - \varphi/2\,\pi \qquad (4)$$

is the fraction of Mercury's solar day (of 176 Earth days) that has elapsed since local noon at the particular longitude (L) of the region under consideration. Combining our 3 mm observations with those of Epstein & Andrew (1985) we arrive at 343 observations, summarized in Fig. 1, which allow an analysis of the brightness temperature Eq. (3) for a finer grid of longitudes. The selected grid is shown in Fig. 1, where $\Delta L = 40°$. The number of observations in the longitude intervals is between 25 and 45, and from the error-weighted least-square method we determined the corresponding parameters $\langle T_B(L)\rangle$, $\Delta T_B(L)$ and $\Omega(L)$ of Eq. (3). With ΔT the error in the determination of T_B, the weighting is made by the percental error $1/(\Delta T/T_B)$. For the majority of the measurements $\Delta T/T_B$ is below 10% (see Table 5). The dependence of the parameters on longitude is shown in Fig. 2, once for the combined data, once for data of this paper. The uncertainties of the parameters shown in Fig. 2 follow from the least-square theory (Bevington 1969).

From the 3/2-locked rotation/revolution it is plausible that the parameters may have, to first order approximation, a $\cos(2\,L + \Theta)$ dependence on L. The corresponding least-square solutions are inserted in Fig. 2. The average temperature $\langle T_B\rangle$ varies between 310 ± 10 K (cool region) and 355 ± 10 K (hot region); the amplitude ΔT_B varies between 110 ± 10 K (cool region) and 150 ± 10 K (hot region). We do not find a 2 L-variation of the phase delay Ω. However the uncertainty in the determination of Ω is large since, for instance, there are only a few observations in the region $240° \lesssim L \lesssim 360°$, $0.3 \lesssim \mathcal{D} \lesssim 0.6$ (Fig. 1).

4. The 150 GHz and 230 GHz interval

The number of observations of the 150 GHz ($N = 40$) and 230 GHz ($N = 62$) interval is too small even for a coarse separation into hot, warm, and cool surface regions. The disk-averaged brightness temperatures irrespective of the surface regions are shown in Fig. 3, the parameters of the best-fit cosine approximations (similar to Eq. (3) but without L-dependence) are given in Table 2. The error of the $\langle T_B\rangle$ term is ±3−15 K; the error of the amplitude term ΔT_B is ±4−20 K; the error of the angle Ω is ±3−7°. The rms-values of the approximations are listed in Table 2.

Our observations at 90 GHz, 150 GHz and 230 GHz are listed in Tables 5 and 6.

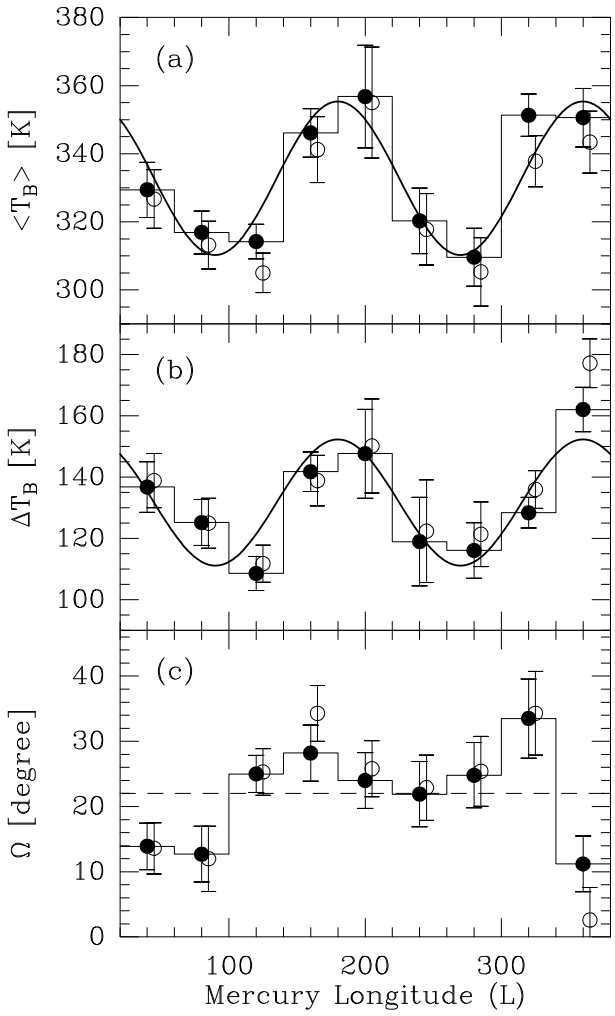

Fig. 2. 90 GHz observations and approximation Eq. (3). Dependence of **a)**: $\langle T_B\rangle$, **b)**: ΔT_B, and **c)**: Ω on longitude L. Dots: combination of our and Epstein & Andrew (1985) data ($N = 343$); open circles: our data ($N = 244$), shown a little displaced in L. The error bars represent the uncertainty of the corresponding parameters. The curves are the least-square $\cos(2L+\Theta)$ approximations, with rms-deviation 5 K **a)**, 6.0 K **b)**. The dashed line in **c)** is the average value.

5. Comparison to model calculations

Models of Mercury's surface layers have been derived from long-term disk-averaged brightness temperature observations, and from several interferometer observations. These observations span the range from cm-wavelengths to 3 mm wavelength. Here we compare the detailed 3 mm observations and the 1.3 to 3 mm observations, combined with longer wavelength data from the literature, with predictions from model calculations.

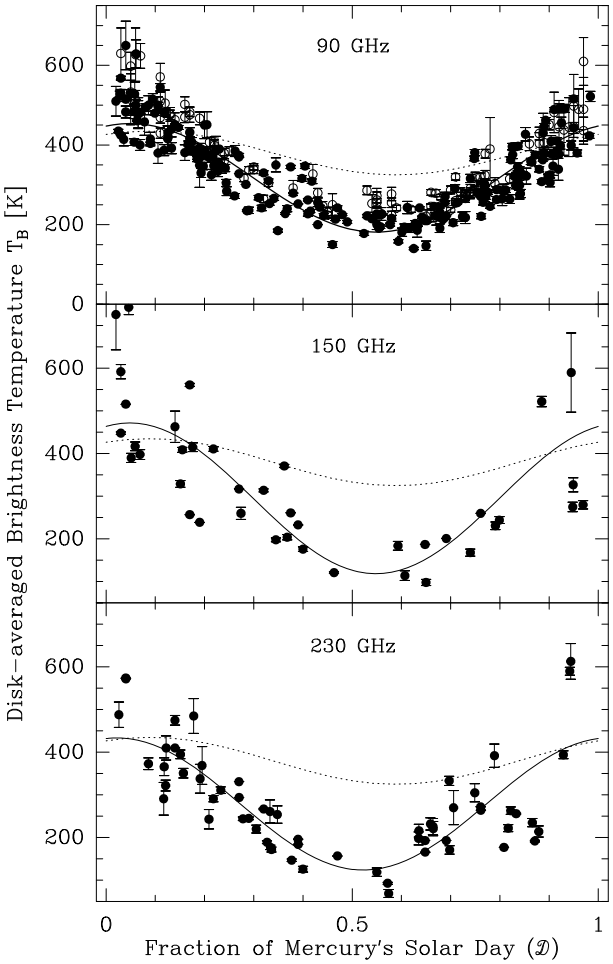

Fig. 3. Disk-averaged brightness temperature at 90 GHz, 150 GHz, and 230 GHz, irrespective of the observed surface region. At 90 GHz: dots our observations, open circles: Epstein & Andrew (1985). The solid lines are cosine approximations (not weighted, Table 2). For comparison the dashed line is the 8 GHz (37.5 mm) observation by Klein (1970), illustrating the smaller brightness temperature variation at longer wavelengths.

We use the thermal model of Mercury's sub-surface developed by Yan et al. (2006) which computes the heat diffusion equation for a grid of longitudes and latitudes of 2° spacing, and 100 vertical layers to 10 m depth. We have combined his thermal model with our radiative transfer code of the sub-surface. This code solves the radiative transfer equation in the sub-surface on a horizontal grid of 100×100 points (the equations are given by Muhleman & Berge 1991; see Eqs. (12), (13) by Mitchell & de Pater 1994). The parameters of the radiative transfer model are (1) the absorption length k_λ, in units of the wavelength λ; (2) the surface dielectric constant ϵ; and (3) the surface roughness, expressed as the rms dispersion of the local surface slope angle, taken to be 15° (see Mitchell & de Pater 1994, Eq. (15)). These calculations give continuum temperature maps of Mercury which are integrated to obtain the disk-averaged brightness temperatures.

In the calculations we use the three models of density and thermal conductivity, as functions of depth, used by Mitchell & de Pater (1994, their Fig. 6), i.e.

– in model A the density and thermal conductivity (k_{350}) are constant with depth;
– in model B the density and thermal conductivity increase continuously with depth;
– in model C the density and thermal conductivity increase abruptly at the depth of 2 cm.

Based on arguments of the relatively small change of ${}^s I_{350}$ (thermal inertia at 350 K) across Mercury's night hemisphere, and agreement of the k_{350} data with lunar data, Mitchell & de Pater (1994) adopt model C as the most realistic one.

Table 2. Cosine-approximation of the unweighted 90 GHz, 150 GHz and 230 GHz observations (Fig. 3), irrespective of surface region.

Freq. (GHz)	$\langle T_B \rangle$ (K)	ΔT_B (K)	Ω (°)	N	rms (K)
90[a]	317	137	17.6	244	19
150	295	176	17.5	40	34
230	278	154	8.5	62	33

[a] Only data of this paper.

Table 3. Parameters used for surface model A,B,C in fitting the observations of Fig. 4.

Model	ϵ	k_λ	tanΔ
A	1.0	20	8×10^{-3}
B	1.5–2.0	20	$5.5–6.5 \times 10^{-3}$
C	1.5	10–15	$9–13 \times 10^{-3}$

5.1. Comparison with the 90 GHz observations

For comparison of the 90 GHz observations with model calculations we select the cool surface regions between $70° \le L \le 110°$ and $250° \le L \le 290°$, and the hot surface regions between $340° \le L \le 20°$ and $160° \le L \le 200°$, all of 40° width as used in Figs. 1 and 2. The result is shown in Fig. 4. Our observations, and those of Epstein & Andrew (1985), show significant scatter; this scatter is not reduced when considering separately the cool regions C 1 and C 2, and the hot regions H 1 and H 2 (Fig. 4).

For the hot region, four "anomalous" data points ($600\,\mathrm{K} < T_B$) coincide with noon time; the measurements are made within ±7 days from upper conjunction. The measurements made by Epstein & Andrew (1985) are in addition marked as being corrected for contamination by solar radiation. These "anomalies" occurred when observing the hot region H 1 *and* H 2. The recurrence of these "anomalies" suggests a real, though unexplained effect.

The parameters used for the models A, B, C that best fit the observations of Fig. 4 are summarized in Table 3. Model A gives systematically too low temperatures during night time, characteristic of a thermal inertia that is too high in the surface layers. Model B and C, with the parameters of Table 3, give the best compromise for the night time temperatures. The corresponding parameters of Table 3 agree with the values obtained by Mitchell & de Pater (1994) for wavelengths shorter than 30 mm.

5.2. Comparison from 230 GHz to 8 GHz

We use the new data in a study of Mercury's disk-averaged brightness temperature as a function of wavelength. We concentrate on the temperatures at midnight ($\mathcal{D} \approx 0.5$) since at this time the temperature difference between the hot, warm and cool surface regions are smallest (~20 K at 3 mm and longer wavelengths, or ~10% and ~5% of the night time brightness

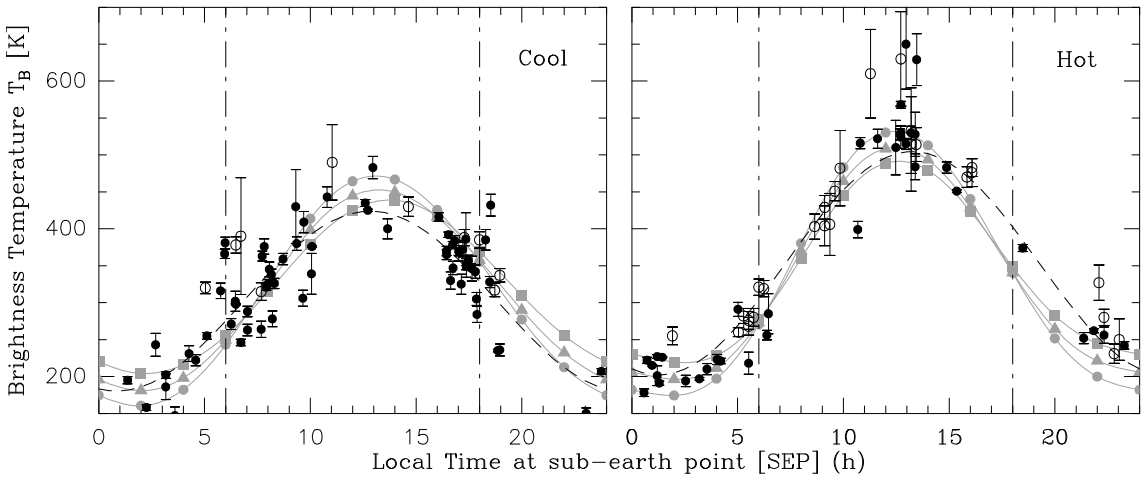

Fig. 4. 90 GHz disk-averaged brightness temperature. Comparison of model calculations and observations, for the cool surface regions $L(\mathrm{C\,1})$ = 70−110° and $L(\mathrm{C\,2})$ = 250−290° and the hot surface regions $L(\mathrm{H\,1})$ = 340−20° and $L(\mathrm{H\,2})$ = 160−200°. Black dots: observations in this paper, open circles: observations by Epstein & Andrew (1985). The dashed lines are the best-fits to our observations (excluding the values with 600 K < T_B; hot region). The grey lines are predictions for the surface model A: dots, B: triangles, C: squares.

Table 4. Mercury: $\langle T_B \rangle$ and ΔT_B as a function of frequency/wavelength, for cosine approximations irrespective of Mercury's surface regions.

Frequency ν (GHz)	Wavelength λ [mm]	$\langle T_B \rangle$ [K]	ΔT_B [K]	Ω [°]	Ref.
8	37.5	380 ± 4	55 ± 3	32 ± 4	1
10.7	28	374 ± 4	42 ± 5	36 ± 7	2
90.0	3.3	359 ± 4	147 ± 6	17 ± 2	2
90	3.5–2.6	317 ±3	137 ± 4	17.6	3
142.8	2.1	350 ± 20	150 ± 15	20	4, in 2
150	1.9–2.1	295 ± 19	176 ± 23	17.5	3
230	1.2–1.4	278 ± 10	154 ± 15	8.2	3

Ref. 1: Klein (1970), Eq. (1); 2: Epstein & Andrew (1985); 3: this paper; 4: Davis (in 2).

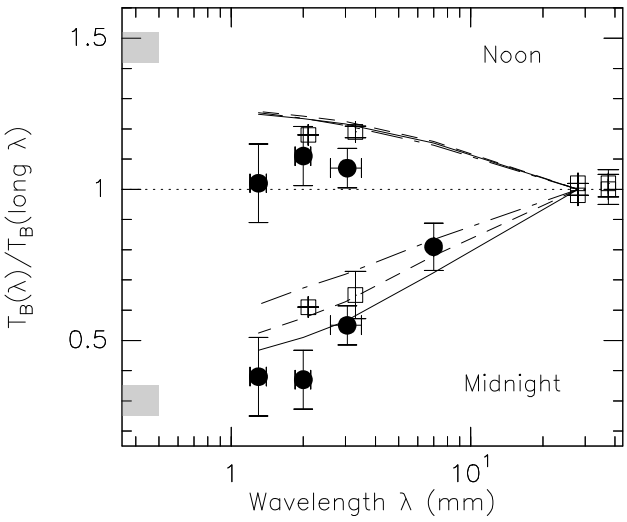

Fig. 5. Ratios of the disk-averaged brightness temperatures at 8, 43, 90, 150, 230 GHz, at the night side (midnight, $\mathcal{D} \approx 0.5$) and at the noon side ($\mathcal{D} \approx 0$ and 1), normalized to the long wavelength observation by Klein (1970, 37.5 mm) and Epstein & Andrew (1985, 28 mm). Solid dots: observations in this paper; open squares: data from the literature, see Table 4. The grey area at the left is the limiting value for the boundary layer. The lines show the model calculations (averaged over the cool, warm, and hot region), continuous line: model A, dashed line: model B, dash-dotted line: model C.

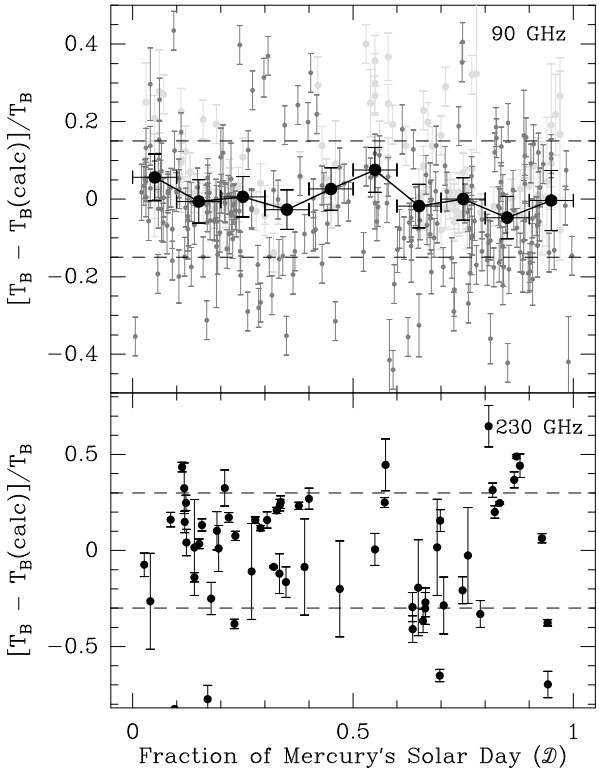

Fig. 6. Mercury as a calibration source at 90 GHz and 230 GHz. T_B is the measured brightness temperature, T_B(calc) the calculated brightness temperature using Eq. (2) at 90 GHz and the parameters of Table 2 at 230 GHz. The errors are those of Tables 5 and 6. The dark symbols are the observations of this paper, the grey symbols those of Epstein & Andrew (1985); the heavy symbols are averages of $\Delta\mathcal{D}$ = 0.1 wide intervals.

temperature at short and long wavelengths). The data used are summarized in Table 4. The listed values $\langle T_B \rangle$ and ΔT_B are obtained from cosine approximations, irrespective of Mercury's surface region, given in the corresponding references of the table; from these values we calculate the midnight temperatures $\langle T_B \rangle - \Delta T_B$. These temperatures are ratioed against a representative temperature at long wavelength; the ratios are shown

Table 5. Mercury at 90 GHz: Brightness temperature T_B [K] (and 1σ error in %). DMY = day, month, year. L = longitude (°) of sub-earth point, $\mathcal{D}$ = fractional day, Eq. (4).

DMY	T_B	$L, \mathcal{D}$	DMY	T_B	$L, \mathcal{D}$	DMY	T_B	$L, \mathcal{D}$	DMY	T_B	$L, \mathcal{D}$
6 1 86	404(4)	210/0.09	25 11 93	349(17)	296/0.19	6 8 98	158(6)	100/0.59	3 11 1	384(6)	118/0.18
22 1 86	483(7)	284/0.04	11 11 94	432(6)	303/0.17	19 8 98	256(8)	189/0.43	11 11 1	497(6)	156/0.11
12 3 86	216(7)	159/0.58	15 4 96	285(9)	69/0.81	15 10 98	339(12)	102/0.92	6 2 2	185(5)	245/0.35
15 7 86	207(5)	82/0.49	16 4 96	263(7)	74/0.79	21 10 98	322(5)	130/0.90	14 4 2	491(5)	204/0.93
31 7 86	262(5)	189/0.41	16 4 96	288(6)	74/0.79	24 10 98	363(4)	144/0.89	15 4 2	492(6)	208/0.92
20 8 86	405(4)	297/0.17	20 4 96	366(5)	93/0.75	18 2 99	378(5)	30/0.91	22 4 2	397(6)	234/0.84
6 1 87	435(5)	280/0.03	27 4 96	245(6)	129/0.68	27 6 99	195(6)	322/0.73	23 4 2	396(6)	242/0.82
27 4 87	515(6)	134/0.09	3 9 96	231(8)	74/0.68	18 7 99	113(7)	83/0.59	28 6 2	305(6)	261/0.24
10 8 87	545(5)	321/0.11	8 9 96	202(6)	105/0.63	12 8 99	268(6)	244/0.31	3 7 2	285(8)	285/0.92
17 8 87	568(4)	350/0.03	18 9 96	178(6)	175/0.52	14 8 99	235(4)	255/0.29	4 7 2	392(4)	289/0.19
17 5 88	220(9)	293/0.72	2 11 96	801(5)	46/0.00	25 8 99	444(5)	307/0.15	14 8 2	278(7)	102/0.84
8 5 90	150(8)	77/0.46	2 4 97	302(8)	82/0.77	29 8 99	480(5)	324/0.10	1 9 2	256(6)	189/0.77
12 6 90	368(5)	273/0.21	14 4 97	203(7)	147/0.63	2 9 99	484(7)	340/0.06	11 9 2	205(7)	243/0.70
26 6 90	494(5)	333/0.08	15 4 97	191(9)	153/0.62	10 9 99	522(6)	14/0.98	16 12 2	375(5)	25/0.87
27 6 90	480(12)	337/0.06	18 4 97	120(14)	172/0.58	4 10 99	308(5)	121/0.88	29 12 2	381(6)	89/0.75
27 8 90	147(12)	265/0.65	21 4 97	201(10)	191/0.55	13 11 99	227(4)	164/0.85:	2 1 3	271(7)	112/0.69
16 10 90	530(5)	188/0.03	23 5 97	301(4)	30/0.28	28 4 0	388(5)	135/0.97	28 3 3	399(6)	198/0.94
23 12 90	222(5)	170/0.53	6 6 97	378(5)	97/0.20	2 6 0	271(4)	281/0.76	30 3 3	456(7)	207/0.93
3 1 91	279(4)	248/0.38	6 6 97	347(6)	97/0.20	13 6 0	255(5)	337/0.69	20 4 3	191(9)	304/0.68
16 2 91	400(7)	105/0.07	9 6 97	407(6)	111/0.17	15 6 0	221(5)	348/0.68	27 4 3	194(8)	345/0.61
11 4 91	227(5)	5/0.55	6 9 97	309(5)	202/0.42	16 6 0	223(7)	353/0.67	2 5 3	191(5)	17/0.55
16 4 91	225(5)	39/0.48	7 9 97	347(5)	209/0.40	19 6 0	210(4)	11/0.65	13 6 3	349(8)	264/0.22
10 6 91	495(4)	331/0.08	8 9 97	316(6)	216/0.40	1 7 0	195(6)	86/0.56	13 6 3	352(6)	264/0.22
25 6 91	489(5)	31/0.91	9 9 97	345(5)	223/0.38	17 7 0	252(4)	192/0.39	14 6 3	372(6)	269/0.22
28 6 91	378(7)	43/0.89	11 9 97	350(9)	235/0.34	29 7 0	328(4)	259/0.27	15 6 3	370(7)	274/0.21
25 7 91	218(10)	168/0.73	27 9 97	416(11)	315/0.12	18 8 0	515(4)	347/0.04	16 6 3	384(5)	279/0.20
22 11 91	298(4)	73/0.77	27 9 97	431(12)	315/0.13	8 9 0	306(7)	76/0.90	17 7 3	462(5)	46/0.89
7 1 92	451(4)	351/0.14	29 9 97	500(8)	32/0.10	11 10 0	281(6)	236/0.75	17 6 3	330(7)	283/0.19
20 1 92	415(8)	51/0.09	29 9 97	380(10)	32/0.11	18 10 0	222(4)	276/0.69	18 6 3	370(5)	288/0.19
13 4 92	310(5)	132/0.33	1 10 97	500(8)	333/0.09	2 11 0	223(6)	21/0.44	20 6 3	404(5)	296/0.17
14 4 92	330(5)	138/0.32	2 10 97	458(11)	337/0.08	15 11 0	330(5)	101/9.72	14 7 3	410(5)	34/0.92
30 4 92	390(4)	222/0.23	4 10 97	629(9)	345/0.06	15 12 0	414(7)	241/0.04	25 7 3	326(6)	81/0.85
12 5 92	416(5)	278/0.17	9 10 97	528(5)	7/0.03	1 2 1	255(5)	103/0.71	26 7 3	338(6)	86/0.84
29 5 92	524(6)	349/0.03	26 10 97	409(7)	83/0.90	21 5 1	211(6)	170/0.02	27 7 3	345(6)	90/0.84
5 6 92	516(5)	17/0.95	28 10 97	380(6)	92/0.89	23 5 1	322(5)	178/0.01:	28 7 3	321(5)	94/0.83
11 6 92	447(5)	41/0.89	20 11 97	322(10)	200/0.85	24 5 1	286(15)	182/0.99	29 7 3	376(6)	99/0.83
15 6 92	427(7)	58/0.85	30 11 97	246(5)	250/0.78	1 6 1	197(4)	0/0.63	30 7 3	363(5)	104/0.82
25 8 92	386(13)	101/0.22	29 12 97	236(7)	80/0.29	2 6 1	140(6)	6/0.62	1 8 3	287(6)	113/0.81
1 9 92	440(8)	131/0.13	24 12 97	228(4)	48/0.36	5 6 1	181(9)	25/0.60	2 8 3	285(9)	118/0.81
8 9 92	528(9)	161/0.06	27 10 97	443(7)	88/0.95	19 6 1	214(5)	116/0.47	11 8 3	285(13)	161/0.77
14 9 92	510(11)	186/0.02	2 1 98	284(7)	102/0.25	23 6 1	244(6)	143/0.43	26 8 3	213(5)	242/0.68
23 9 92	380(6)	225/0.96	3 1 98	346(8)	108/0.23	4 7 1	266(6)	210/0.34	27 8 3	220(6)	248/0.68
2 10 92	376(4)	266/0.92	4 1 98	334(8)	113/0.23	7 7 1	242(6)	227/0.32	1 9 3	186(13)	267/0.63
13 10 92	339(5)	316/0.88	5 1 98	348(9)	118/0.22	8 7 1	445(6)	232/0.31	6 9 3	200(5)	313/0.58
7 11 92	316(7)	81/0.74	2 4 98	226(4)	173/0.56	9 7 1	431(6)	237/0.30	15 10 3	407(6)	171/0.06:
16 12 92	381(9)	323/0.16	4 4 98	215(4)	187/0.54	12 7 1	432(7)	253/0.27	16 10 3	530(5)	176/0.05
23 12 92	483(5)	357/0.12	6 5 98	370(4)	24/0.27	13 7 1	385(7)	258/0.26	30 10 3	423(5)	238/0.98
23 12 92	750(6)	357/0.12	7 5 98	272(6)	29/0.26	15 7 1	492(5)	267/0.24	20 11 3	347(10)	339/0.91
4 1 93	482(4)	32/0.07	21 5 98	365(5)	95/0.19	16 7 1	348(5)	273/0.23	20 12 3	219(5)	335/0.64
5 1 93	477(11)	57/0.06	29 5 98	420(10)	130/0.13	20 7 1	369(4)	291/0.19	31 12 3	234(5)	209/0.41
6 1 93	461(4)	62/0.06	27 6 98	299(8)	248/0.84	22 7 1	398(6)	299/0.17	5 1 4	253(5)	243/0.33
7 1 93	500(6)	66/0.06	28 6 98	325(5)	253/0.83	16 8 1	398(6)	43/0.92	24 1 4	320(5)	346/0.17
15 1 93	425(4)	103/0.03	30 6 98	264(8)	262/0.82	17 8 1	386(5)	47/0.92	1 2 4	392(7)	24/0.13
10 3 93	242(6)	15/0.47	8 7 98	281(5)	299/0.78	19 8 1	377(7)	56/0.91	1 5 4	240(7)	126/0.37
14 3 93	200(4)	44/0.43	9 7 98	269(5)	303/0.77	20 8 1	325(6)	60/0.90	8 6 4	387(7)	316/0.12
16 3 93	227(6)	57/0.41	10 7 98	273(5)	308/0.76	23 8 1	430(15)	73/0.89	3 7 4	357(6)	57/0.87
3 4 93	374(5)	165/0.27	21 7 98	291(7)	4/0.71	29 8 1	359(6)	100/0.86	22 7 4	221(6)	145/0.76
16 4 93	451(11)	230/0.20	28 7 98	246(6)	44/0.67	4 9 1	275(7)	128/0.84	11 9 4	342(6)	93/0.24
25 8 93	650(13)	167/0.04	30 7 98	210(6)	56/0.65	5 9 1	317(6)	133/0.84	12 9 4	357(6)	98/0.23
16 4 93	450(11)	230/0.20	1 8 98	242(5)	68/0.64	6 9 1	298(6)	138/0.83	13 9 4	325(8)	102/0.21
19 11 93	558(9)	265/0.26:	4 8 98	243(10)	87/0.61	11 9 1	228(10)	162/0.81:	15 9 4	385(5)	112/0.19

in Fig. 5. Following Table 4, for midnight the 8 GHz/37.5 mm observation by Klein (1970) gives 325 K, the 10.7 GHz/28 mm observation by Epstein & Andrew (1985) gives 332 K; we adopt as the average for the long wavelengths T_B(long λ, night)=330 K.

Table 6. Mercury at 150 GHz and 230 GHz: Brightness temperature T_B [K] (and 1σ error in %). DMY = day, month, year. $\mathcal{D}$ = fractional day, Eq. (4).

DMY	T_B	$\mathcal{D}$	DMY	T_B	$\mathcal{D}$	DMY	T_B	$\mathcal{D}$	DMY	T_B	$\mathcal{D}$
150 GHz											
7 6 89	261(15)	0.38	15 1 93	448(15)	0.03	29 7 0	317(15)	0.27	6 8 3	231(18)	0.79
24 7 89	590(30)	0.94	13 11 93	371(15)	0.36	18 8 0	516(15)	0.04	25 2 4	743(17)	0.05
27 8 90	98(22)	0.65	19 11 93	545(15)	0.26	1810 0	201(15)	0.69	1 5 4	204(17)	0.37
30 10 90	280(18)	0.97	25 11 93	239(15)	0.19	27 6 1	176(18)	0.40	8 5 4	314(16)	0.32
5 11 90	327(20)	0.95	11 11 94	561(15)	0.17	12 8 1	275(19)	0.95	23 12 4	260(20)	0.27
16 2 91	398(17)	0.07	15 10 96	411(16)	0.22	14 9 1	244(18)	0.80	21 3 5	184(20)	0.59
7 1 92	463(22)	0.14	28 7 99	121(16)	0.46	1 4 2	390(17)	0.05	14 4 5	198(17)	0.34
12 5 92	257(15)	0.17	28 7 99	121(16)	0.46	18 4 2	522(17)	0.88	29 5 5	417(17)	0.06
29 5 92	592(17)	0.03	2 6 0	260(15)	0.76	16 2 3	409(16)	0.16	27 7 5	114(24)	0.61
14 9 92	726(26)	0.02	19 6 0	187(15)	0.65	17 2 3	329(17)	0.15			
7 11 92	168(19)	0.74	17 7 0	233(15)	0.39	19 6 3	415(17)	0.18			
230 GHz											
27 4 87	805(15)	0.09	16 3 92	216(21)	0.64	21 4 97	119(23)	0.55	26 7 1	322(18)	0.12
8 3 88	468(17)	0.23	17 3 92	198(22)	0.63	1 10 97	373(18)	0.09	16 6 2	177(18)	0.33
16 3 88	369(27)	0.19	14 4 92	267(15)	0.32	15 11 97	214(21)	0.88	17 6 2	189(16)	0.33
17 3 88	338(24)	0.19	23 12 92	291(28)	0.12	8 6 98	488(21)	0.03	20 6 2	220(19)	0.31
30 6 88	254(22)	0.35	5 2 93	394(17)	0.93	29 7 98	232(21)	0.66	22 6 2	245(16)	0.29
16 5 89	(69:)(28)	0.57	15 2 93	256(15)	0.83	19 12 98	291(17)	0.22	24 6 2	244(16)	0.28
12 6 90	243(24)	0.21	10 3 93	157(15)	0.47	27 8 99	410(21)	0.12	17 2 3	395(17)	0.15
11 1 91	311(17)	0.23	11 2 93	475(17)	0.14	2 6 0	272(15)	0.76	31 7 3	222(18)	0.82
7 1 92	410(15)	0.14	9 3 94	333(18)	0.70	19 6 0	193(15)	0.65	24 8 3	171(20)	0.70
21 2 92	590(16)	0.94	2 4 94	485(23)	0.18	17 7 0	196(15)	0.39	28 11 3	192(16)	0.87
21 2 92	728(21)	0.94	7 4 94	351(18)	0.16	29 7 0	331(15)	0.27	29 11 3	235(19)	0.87
6 3 92	392(21)	0.79	3 5 94	613(21)	0.94	18 8 0	574(15)	0.04	7 2 4	245(17)	0.11
9 3 92	305(22)	0.75	11 11 94	700(22)	0.17	29 9 0	263(18)	0.82	6 5 4	261(25)	0.33
12 3 92	270(29)	0.71	25 9 96	147(16)	0.38	2 10 0	111(25)	0.81	8 6 4	366(20)	0.12
14 3 92	221(22)	0.66	11 1 97	172(18)	0.34	18 10 0	193(15)	0.69			
15 3 92	226(23)	0.66	19 4 97	93(17)	0.57	27 6 1	126(20)	0.40			

The 8 GHz observations by Klein are calibrated against Cyg A of 214 Jy which is 6% higher than the flux density given by Baars et al. (1977). The observations by Epstein & Andrew are calibrated against several quasars, which are also compared against Cyg A (with flux density taken from Baars et al. 1977); they estimate the absolute error in the measurements to be 5%. Taking into account the cosine approximation of the observations from which the midnight brightness temperature is derived, we estimate that the error in the value $T_B(\text{long}\,\lambda, \text{night}) = 330$ K does not exceed 10 to 15%.

Similar ratios for noon time ($\mathcal{D} \approx 0$ and 1) are also shown in Fig. 5. The long wavelength value is again derived from the Klein (1970) 8 GHz observation and the Epstein & Andrew (1985) 10.7 GHz observation; the adopted value is $T_B(\text{long}\,\lambda, \text{noon}) = 425$ K. The noon values $\langle T_B \rangle + \Delta T_B$ are obtained from the data of Table 4.

A measurement of Mercury with the IRAM 30-m telescope at 43 GHz (7 mm) was made in July 9–13, 1993 (Greve et al. 1994). The observations fall in the time of midnight ($0.537 \leq \mathcal{D} \leq 0.564$) of the cool surface region. The measured brightness temperature is $T_B(43) = 265 \pm 20$ K. The data are used in Fig. 5.

When we use the model calculations of Mercury by Hale & Hapke (2002), the temperature at very short wavelengths (say $\lambda \approx 0.3$ mm) and thus of the surface boundary layer is $T(\text{night}) \approx 90$–$110$ K and $T(\text{noon}) \approx 600$–$650$ K (their Fig. 16). The limiting values at the boundary layer is $T(\text{night})/T(\text{long}\,\lambda, \text{night}) \approx 100/330 = 0.30$ and $T(\text{noon})/T(\text{long}\,\lambda, \text{noon}) \approx 625/425 = 1.47$. These ratios are shown in Fig. 5.

The calculations for model A, B and C are inserted in Fig. 5. The calculated disk-averaged brightness temperatures are the averages for the hot, warm and cool surface regions, for midnight time and noon time. We notice that the ratios for noon time do not discriminate between model A, B, and C. The ratios at midnight time are closer to the prediction from model A and B, although we are aware that the measured ratios may shift in vertical direction depending on the adopted values $T(\text{long}\,\lambda, \text{midnight})$ and $T(\text{long}\,\lambda, \text{noon})$. However, for an error of ±10% in the values $T(\text{long}\,\lambda)$ this shift does not exceed ±0.1.

6. Mercury as a calibration source

Comparing the measured 90 GHz brightness temperatures $T_B(\mathcal{D}, L)$ (Table 5 and Epstein & Andrew (1985) measurements) with brightness temperatures calculated from Eq. (2) for the values $\mathcal{D}, L$ we find for the 340 observations a deviation of 15% (rms), or less. Mercury can be used at any position $(\mathcal{D}, L)$ with this precision as a 90 GHz calibrator when using in Eq. (2): $\langle T_B \rangle = 332{+}22.5\cos(2L)$ (K) and $\Delta T_B = 131{+}20.5\cos(2L)$ (K) (Fig. 2). The normalized differences between the measured values $T_B(\mathcal{D}, L)$ and the values $T_B(\text{calc})$ calculated from the theoretical relation Eq. (2) are shown in Fig. 6.

At 150 GHz the number of observations is too small to derive an analytic relation for calibration. At 230 GHz the parameters of Table 2 define a relation averaged over all longitudes. Using that relation for calibration the error is of the order of 25 to 30%. Additional observations are required to obtain a better longitude coverage.

For a given frequency there occurs at night time ($\mathcal{D} \approx 0.5$) the smallest difference in brightness temperature between the different surface region. When using the parameters of Table 2, a calibration with higher precision is obtained for this period.

7. Summary

This paper presents single-dish observations of Mercury at 90 GHz, 150 GHz, and 230 GHz. We have analysed the observations as a function of Mercury's solar day, at 90 GHz also as a function of Mercury's longitude. Unfortunately, at 150 GHz and 230 GHz the number of observations is still too small to allow even a course separation into hot, warm, and cool surface regions. We obtain the following results:

1. At 90 GHz the disk-average brightness temperature $\langle T_B \rangle$ and the amplitude ΔT_B are cosine-form variations of Mercury's solar day and functions of Mercury's longitude, as shown in Fig. 2. The figure illustrates that there exists a consistency between our 3 mm observartions and those of Epstein & Andrew (1985). The errors of $\langle T_B \rangle(L)$ and $\Delta T_B(L)$ (for $\Delta L = 40^o$) in Figs. 2a, b are of the order of 20 K. Local deviations of Mercury's brightness temperature in 40^o wide longitude zones from a cosine(2 Longitude) dependence apparently do not exceed $\sim\sqrt{2} \cdot 20 \approx 30$ K.
2. The 90 GHz observations of the cool and hot surface region are compared in Fig. 4 with the predictions from Mercury's surface model A, B, and C used by Mitchell & de Pater (1994). The diurnal temperature veriation is reproduced by models A, B, and C, with the constants of Table 3, however, the scatter of the observations underlines the difficulty in constraining Mercury's surface models from single-dish observations.
3. Figure 5 shows the dependence of the ratio $\mathcal{R} = T_B(\lambda)/T_B(\text{long } \lambda)$, where the adopted brightness temperature at long wavelengths is 330 K for midnight time, and 425 K for noon time. The long wavelength brightness temperatures are derived from the 8 GHz (37.5 mm) observation by Klein (1970) and the 10.7 GHz (28 mm) observation by Epstein & Andrew (1985). For the night side ($\mathcal{D} \approx 0.5$) the predictions from model A and B suggest a better agreement with the measured ratios $\mathcal{R}$, while the ratios on the noon side do not allow a discrimination between the models. The figure illustrates that in this context the 2 mm (150 GHz) and 1.3 mm (230 GHz) observations are very important. Additional observations at these wavelengths, and shorter wavelengths, taken during Mercury's night time ($\mathcal{D} \approx 0.5$) are required to confirm the short wavelength behaviour shown in Fig. 5.

The 90 GHz brightness temperatures T_B of this paper, and their errors (1σ), are given in Table 5 (values denoted by: are uncertain, and disregarded in Fig. 4); the 150 GHz and 230 GHz brightness temperatures are given in Table 6. Following Sect. 2, if no other determination is available, we have entered a minimum error (1σ) of 5% in Table 5 (90 GHz), and 15% in Table 6 (150 GHz, 230 GHz). The tables are available from CDS.

Acknowledgements. During the 20 years 1985–2005, many staff astronomers and operators of the 30 m telescope contributed to the collection of the data presented here. We thank the many colleagues for their contribution which, unnoticed by most of them, allowed the collection of these data. J. Peñalver (IRAM, Spain) helped in retrieving the archived observations. We thank the referee(s) for the comments, and the patience with this paper.

References

Altenhoff, W. J., Baars, J. W. M., Schraml, J., et al. 1996, A&A, 309, 953
Baars, J. W. M., Genzel, R., Pauliny-Toth, I. I. K., & Witzel, A. 1977, A&A, 61, 99
Bevington, P. R. 1969, Data Reduction and Error Analysis for the Physical Sciences (New York: McGraw-Hill Book Comp.)
Cuzzi, J. N. 1974, ApJ, 189, 577
Downes, D. 1989, in Evolution of Galaxies; Astronomical Observations, ed. J. Appenzeller, H. J. Habing, & P. Lena, Lecture Notes in Physics, 333, 351
Epstein, E. E., Dworetsky, M. M., Fogarty, W. G., Montgomery, J. W., & Cooley, R. C. 1970, Radio Sci., 5, 401
Epstein, E. E., & Andrew, B. H. 1985, Icarus, 62, 448
Greve, A., Steppe, H., Graham, D. A., & Schalinski, C. J. 1994, A&A, 286, 654
Greve, A., Neri, R., & Sievers, A. 1998a, AA&S, 132, 413
Greve, A., Kramer, C., & Wild, W. 1998b, AA&S, 133, 271
Greve, A., Bremer, M., Penalver, J., Raffin, P., & Morris, D. 2005, IEEE Trans. Ant. Propagat., AP-53, 851
Hale, A. S., & Hapke, B. 2002, Icarus, 156, 318
Ingersoll, A., Svitek, T., & Murray, B. 1992, Icarus, 100, 40
Keihm, S. J. 1984, Icarus, 60, 568
Klein, M. J. 1970, Radio Sci., 5, 397
Krotikov, V. D., & Troitskii, V. S. 1964, Sov. Phys. Usp., 6, 841
Krotikov, V. D., & Shchuko, O. B. 1975, Sov. Astron., 19, 86
Ledlow, M. J., Burns, J. O., Gisler, G. R., et al. 1992, ApJ, 384, 640
Linsky, J. L. 1973, ApJS, 25, 163
Mitchell, D. L., & de Pater, I. 1994, Icarus, 110, 2
Morrison, D. 1970, Space Sci. Rev., 11, 271
Morrison, D., & Klein, M. J. 1970, ApJ, 160, 325
Muhleman, D. O., & Berge, G. L. 1991, Icarus, 92, 263
Olmi, L. 2001, A&A, 374, 348
Peale, S. J. 1988, in Mercury, ed. F. Vilas, C. R. Chapman, & M. S. Matthews (Tucson: University of Arizona Press)
Perley, R. A., Zijlstra, A., & van Hoof, P. 2006, BAAS, 38, 1028
Reuter, H. P., & Kramer, C. 1998, A&A, 339, 183
Salvail, J., & Fanale, F. 1994, Icarus, 111, 441
Sanchez-Contreras, C., Alcolea, J., Bujarrabal, V., & Neri, R. 1998, A&A, 337, 233
Sandell, G. 1994, MNRAS 271, 75
Soter, S. L., & Ulrichs, J. 1967, Nature, 214, 1315
Sprague, A., Hunten, D., & Lodders, K. 1995, Icarus, 118, 211
Vasavada, A., Paige, D., & Wood, S. 1999, Icarus, 141, 179
Steppe, H., Paubert, G., Sievers, A., et al. 1993, AA&S, 102, 611
Yan, N., Chassefiere, E., Leblanc, F., & Sarkissian, A. 2006, Adv. Space Res., 38, 583